

Synergetic Protection Hollow Silicon by Nitrogen-Doped Carbon/Reduced Graphene Oxide to Improve the Electrochemical Stability as Lithium-Ion Battery Anode

Yan Ma¹, Yunxia Liu¹, Mingshan Wang^{1,*}, Zhenliang Yang², Yongshun Bai¹, Xue Yin¹, Chun Luo¹, Yun Huang¹, Xing Li^{1,*}

¹ The Center of New Energy Materials and Technology, School of Materials Science and Engineering, Southwest Petroleum University, Chengdu, Sichuan 610500, P.R. China

² Institute of Materials, China Academy of Engineering Physics, Mianyang, Sichuan 621908, PR China

*E-mail: wangmingshan@swpu.edu.cn, lixing@swpu.edu.cn

Received: 5 March 2019 / Accepted: 12 April 2019 / Published: 10 May 2019

Silicon is the most sought-after candidates for next-generation electrode materials for high energy density lithium ion battery because of its high theoretical capacity and appropriate working potential. However, it still suffers from dramatic volume expansion/shrinkage during repeat discharge/charge process, along with unstable solid electrolyte interface films, which largely degrade its practical application. To overcome these problems, we present an approach to synthesize hollow silicon@nitrogen-doped carbon/reduced graphene oxide (H-Si@N-C/rGO) composite via polymerization coating with dopamine on hollow Si and hydrothermal with graphene oxide followed by thermal reduction. The hollow structure of Si and intragranular voids between the Si nanoparticles significantly relief the volume change during lithiation/delithiation process. The synergetic protecting of nitrogen-doped carbon/reduced graphene oxide also improves the stability of surface of silicon. As a result, the H-Si@N-C/rGO composite delivers initial reversible capacity of 818 mAh g⁻¹ with retains 92% of initial capacity after 100 cycles at a current density of 0.2 A g⁻¹, and also displays stable cycling performance at a high current density of 1 A g⁻¹.

Keywords: Hollow silicon; Dopamine; Graphene; Lithium ion battery anode

1. INTRODUCTION

The impact of decreasing fossil energy has been risen the concern of development and application of renewable energy[1-3]. The electrochemical power sources techniques for clean-energy conversion system have been extensively researched during the past decades, such as lead-acid battery, MH-Ni battery, and Cd-Ni battery. Among them, lithium-ion batteries (LIBs) has been widely applied since its

first commercial application by SONY Company in 1990. The typical anodes materials for LIBs is graphite, which can hosts lithium ion as LiC_6 with theoretical capacity of 372 mAh g^{-1} . However, with the development of energy storage markets in electronic vehicles, exploration of new materials with higher energy density, safer performance to meet the imperative demands have attracted enormous attention[4, 5]. Silicon has been considered as a promising anode material due to its high theoretical capacity ($\sim 3572 \text{ mA h g}^{-1}$ with formation $\text{Li}_{15}\text{Si}_4$ at ambient temperature)[6], low discharge potential (0-0.4V vs. Li/Li^+) and abundant nature resource (the second abundant element on earth)[7, 8]. However, silicon based anode materials still suffer from rapid capacity degradation caused by the material pulverization and falling from current collector due to the huge volume expansion/shrinkage ($\sim 300\%$) during repeated lithiation/delithiation process. A great many efforts have been made on the design and fabricated novel nanostructured silicon, such as silicon nanowires[9], silicon nanotubes, silicon nanoarray[10], silicon porous structure. Hollow silicon structure has been proved to have favorable mechanical reliability because of alleviating cracks and fractures by accommodating the large volume change[11, 12]. However, the amount of SEI inevitably generated at the surface of silicon, which cause the loss of electrochemical activity during cycling. To overcome the problem, effective strategies of introduction of coating layer such as carbonaceous materials[13-16], conductive polymers[17-19] have been carried out in the previous reports. Such coating layer on the surface of silicon make significant improvement in the electrochemical performance because of suppression the large particles volume expansion due to the ductility of coating layer. At the meantime, the stability of particles interface can be also enhancement by replacement of silicon surface to form more stable SEI layer on coating layer. Therefore, the core-shell silicon-based composites are considered as an effective method for the application of silicon based materials in LIBs. However, the core-shell structure silicon-based materials still meet a great challenge due to the diffusion way of Li-ions and transfer distance of electrons are not maintained if those particles are agglomerated in electrode. Accordingly, there are many efforts focused on ameliorating the agglomeration of particles in composites by dispersion those particles on secondary carbon matrix, such as introduction of carbon fibers[20, 21], carbon cloth[22, 23], carbon paper[24], or graphene[25-28]. The design not only decreases the non-uniform dispersion of active materials, but also improves the chance to shorten the ion transport pathway and facilitate the electrons transfer during the matrix.

Inspired by the design of pervious hollow silicon(H-Si) structure and dual protection strategy[29-31], in this paper, the dual carbonaceous protected H-Si composites are rational designed via polymerization coating with dopamine on H-Si followed by anchoring the H-Si@dopamine on graphene oxide. After hydrothermal and thermal reduction, the H-Si@ nitrogen-doped carbon/reduced graphene oxide (H-Si@N-C/rGO) composite are obtained. For the H-Si@N-C/rGO structure, the hollow structure allows expansion and contraction of Si during the lithiation and delithiation without pulverization. Meanwhile, the carbon layer originating from polydopamine can both encapsulate H-Si and further anchor them to the graphene, forming an integrative structure Si/C composites. Thus, the as-prepared novel H-Si@N-C/RGO composite exhibited high electrochemical performance, which will be investigated in detail as following section.

2. EXPERIMENTAL

2.1. Materials

All the chemicals used were analytical grade. Glucose, methanol, sodium hydroxide (NaOH), absolute ethanol, sodium chloride (NaCl), concentrated ammonium hydroxide ($\text{NH}_3 \cdot \text{H}_2\text{O}$, 25%), hydrochloric acid (HCl, 36%) and tetraethoxysilane (TEOS) were provided by Chengdu Kelong Chemical Reagent Factory. Magnesium powder (1000 mesh) was purchased from Shanghai Naiou Nano technology Co., Ltd. Graphene oxide was obtained from British Shaped Technology Development Co., Ltd.

2.2. Materials synthesis

Synthesis of Carbon spheres template: The 5.8 g/ml aqueous glucose solution with 1.5% methanol was fill in a 100 ml beaker, and the pH was adjusted to 8 with 0.1 M NaOH. Then the mixed solution was sealed into a stainless steel autoclave and hydrothermally treated at 180 °C for 8 h. The obtained carbonaceous materials were collected by vacuum filtration and washed three times with ethanol, followed by a vacuum drying overnight.

Synthesis of hollow silica (H-SiO₂): The hollow silica particles were prepared by modified Stöber method. Typically, the carbonaceous materials (0.2 g) and PVP (1 g) were added to a mixture of 30 mL absolute ethanol and 30 mL deionized water under sonication for 2 h. And then 0.6 g CTAB and 9 mL $\text{NH}_3 \cdot \text{H}_2\text{O}$ was added to above suspension solution under constant stirring at 30 °C. Next, 3 mL TEOS was added to 30 mL absolute ethanol under drastic stirring for 30 min. After that, this solution was dropped into the above suspension solution and stirred for 10 h at 30 °C. The resulting precipitates were collected by vacuum filtration and washed three times with ethanol, and then dried at 70 °C for 12 h. Finally, the prepared products were calcined at 550 °C for 4 h in air to obtain hollow silica (H-SiO₂).

Synthesis of H-Si: The H-Si materials were prepared by modified magnesiothermic reduction[32]. Typically, the H-SiO₂, Mg and NaCl powder were mixed at a mass rate of 1:0.9:10 and sealed into a stainless-steel reactor in an argon-filled glove box. After the reactor was calcined in a tube furnace at 650 °C for 4 h under argon, the mixed powder was added to 100 mL HCl (1 M) under moderate stirring for 30 min to remove MgO. Then the sample was treated with 5% HF for 2 min to obtain hollow silicon.

Synthesis of H-Si@N-C/rGO composite: Firstly, 0.12g H-Si was dispersed into 50 mL dopamine hydrochloride solution (2 mg mL⁻¹). Then, 10mM Tris-buffer (50 mL, pH=8.5) with 40 mg ammonium persulfate was added into the above suspension solution and stirred for 2 h. The obtained H-Si@PDA was collected by vacuum filtration and washed three times with deionized water. Next, the H-Si@PDA was mixed with CTAB (60 mg) in deionized water (30 mL) and stirred for 30 min. And 30 mL GO solution (2 mg mL⁻¹) was dropped into mixture solution and stirred for 3 h. After that, the obtained H-Si@PDA-GO was collected by filtration and freeze drying. Finally, the H-Si@N-C/rGO was prepared by heated treatment at 800 °C for 3 h at a rate of 5 °C min⁻¹ in argon.

Synthesis of Si rGO composite: For comparison, commercially available nano-silicon (Si, 100 nm) was directly hydrothermally reacted with graphene oxide, and then subjected to thermal reduction under the same conditions to obtain a Si/rGO composite.

2.3. Materials characterization

The scanning electron microscope (SEM, ZEISS EV0 MA15) was used to characterize the morphology of materials. X-ray diffraction (XRD) patterns of materials were conducted by DX-2700 diffraction with a high voltage of 40 kV and Cu K α radiation ($\lambda=1.5406\text{\AA}$). The structures of prepared materials were carried out using Fourier transform infrared spectroscopy (FTIR, PerkinElmer Spectrograph) with a wavenumber range of 4000-400 cm^{-1} . The Raman spectra of prepared samples were recorded on ID Raman micro IM-52 with fixed laser wavelength of 785nm. The thermogravimetric analysis (TGA) was measured by Mettler Toledo TGA analyzer in air with a heating rate of 10 $^{\circ}\text{C min}^{-1}$.

2.4. Electrochemical measurements

The tests of half-cell were performed using CR2032-type coin cells with composite material as working electrode, lithium-foil as counter electrode, a Celgard polypropylene film as separator and 1 M LiPF₆ in EC:DEC:FEC (1:1:1, v/v/v) as electrolyte, assembled in an argon-filled glove box. The working electrodes consisted of active material, acetylene black and sodium alginate binder with mass ratio of 7:2:1. Electrochemical performance was tested using a Neware battery measurement system at voltage of 0.01-1.5 V at 30 $^{\circ}\text{C}$. The cycle voltammetry (CV) data were collected using electrochemical workstation (CHI760e) with a scan rate of 0.5 mV s^{-1} . The electrochemical impedance spectroscopy (EIS) tests were conducted in the frequency range of $10^{-2} \sim 10^5$ Hz.

3. RESULTS AND DISCUSSION

Fig. 1 shows the fabrication process and schematic structure of H-Si@N-C/rGO composite. Firstly, C@SiO₂ spheres are fabricated by template method via hydrolysis of TEOS as silicon precursor under alkaline environment using carbon spheres as hard template. Then, the H-Si sphere can be obtained after removal of carbon by high temperature decomposition in air followed by magnesiothermic reduction of SiO₂. During the process, Mg powder can react with silica to form Si and MgO at 650 $^{\circ}\text{C}$ in Ar atmosphere. The residual MgO and Mg powder can be removed by washing the products with HCl. According to the above treatment, the pure H-Si can be obtained. After that, H-Si will further in situ polymerize the dopamine to form H-Si@polydopamine in tris-buffer solution. Then, CTAB was introduced to assist H-Si@polydopamine anchoring on the surface of graphene by hydrothermal reaction. Finally, the H-Si@N-C/rGO can be fabricated by further carbonized graphene oxide and polydopamine under high temperature.

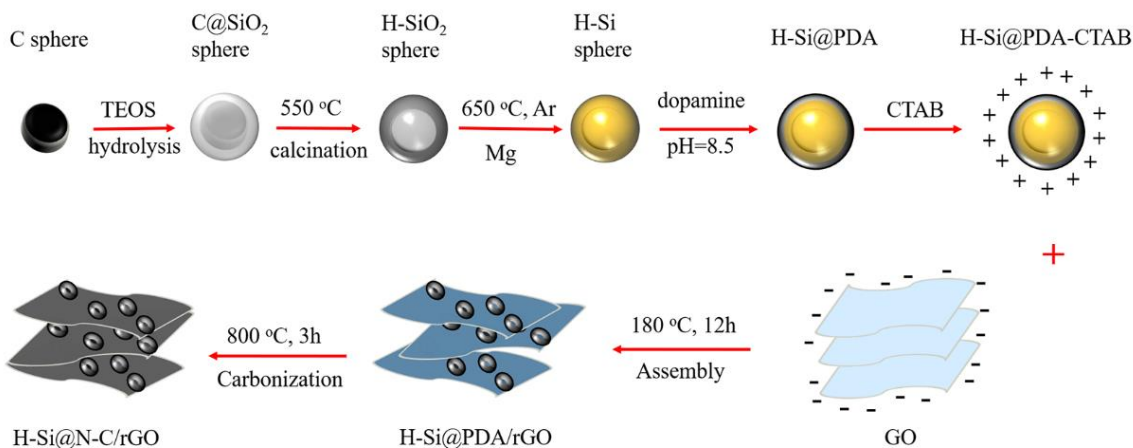


Figure 1. Schematic illustration for the preparation of H-Si@N-C/rGO.

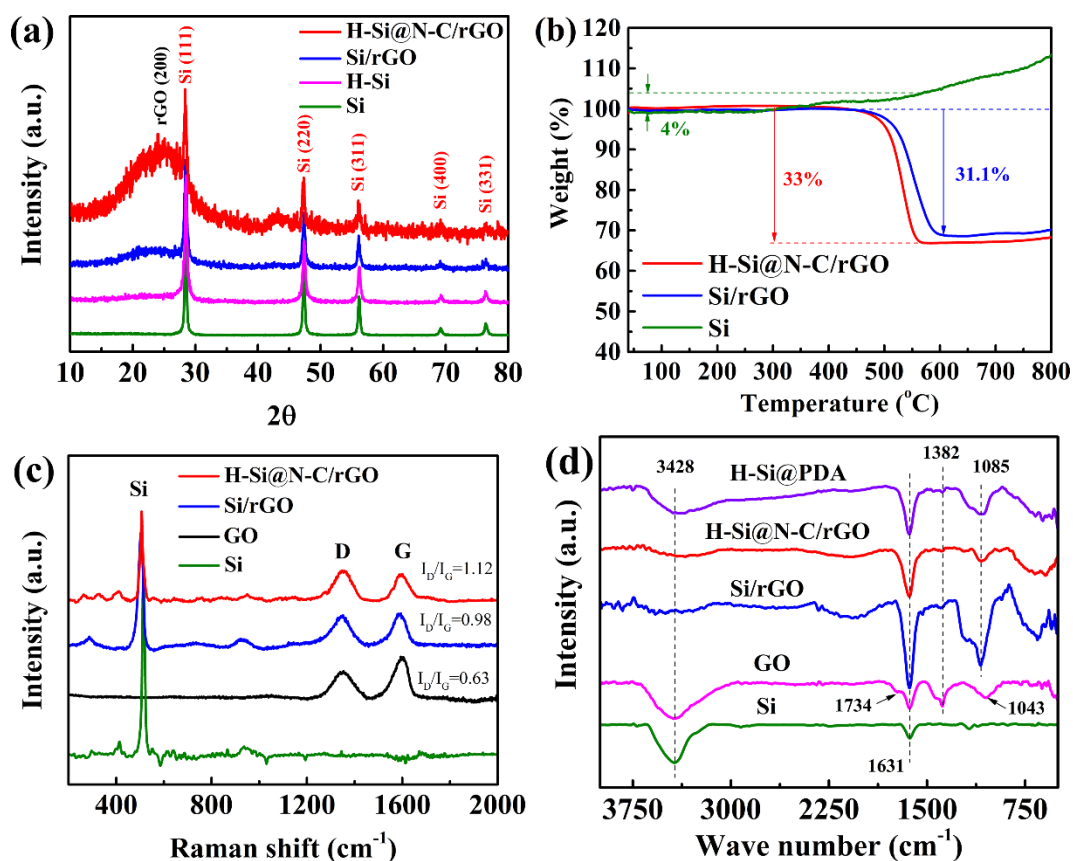


Figure 2. (a) XRD patterns of H-Si@ N-C/rGO, H-Si, Si/rGO, and Si; (b) TGA curves of H-Si@N-C/rGO, Si/rGO, and Si; (c) Raman spectra of H-Si@ N-C/rGO, Si/rGO, GO and Si; (d) FT-IR spectra of H-Si@ N-C/rGO, H-Si@PDA, Si/rGO, GO and Si.

Fig.2a shows the XRD patterns of the Nano-Si, H-Si, Si/rGO and as-prepared H-Si@N-C/rGO, respectively. All diffraction peaks of Nano-Si and H-Si can be indexed to the cubic Si with space groups of Fd-3m (JCPDS: 27-1402) with diffraction peaks at 28.4°, 47.3°, 56.2°, 69.2° and 76.4°, corresponding to the (111), (220), (311), (400) and (331) planes, respectively. This result confirmed that the H-Si is successful obtained by modified magnesiothermic reduction. It also should be noted that the peak

intensity of H-Si@N-C/rGO is relative weak, indicating the nano size of Si particles after magnesiothermic reduction. Meanwhile, a broad peak appears at 25°, which is ascribe to the disordered stacking characteristic of graphene structure and amorphous carbon structure as described in other literature[33]. The carbon content of composites for Si/rGO and H-Si@N-C/rGO are calculated by the TG curves of Fig.2b. The mass of Si gradually increases from about 400 °C, which is caused by the oxidation of Si into SiO₂ in the air. Si/rGO and H-Si@N-C/rGO have a large weight loss phenomenon around 600 °C, which is due to the decomposition of carbon. Thus, according to the data from TG result and considering the weight increased by the oxidation of Si. The carbon content of Si/rGO and H-Si@N-C/rGO can be calculated by the following equation[34]:

$$\frac{X_1 + 4\% * X_1}{X_1 + 4\% * X_1 + 31\%} = 1 - 31\% \rightarrow X_1 = 66\% \quad (\text{Si/rGO})$$

$$\frac{X_2 + 4\% * X_2}{X_2 + 4\% * X_2 + 33\%} = 1 - 33\% \rightarrow X_2 = 64\% \quad (\text{H-Si@N-C/rGO})$$

Where X₁, X₂ is the content of Si in Si/rGO and H-Si@N-C/rGO, respectively. As a result, the carbon contents of Si/rGO and H-Si@N-C/rGO are 34 and 36%, respectively. Raman spectra of H-Si@N-C/rGO, Si, Si/rGO and GO show on Fig. 2c. It can be clearly seen that a strong peak appears around 510 cm⁻¹, which corresponds to the Raman peak of crystalline silicon. Two Raman peaks appear at 1350 cm⁻¹ and 1591 cm⁻¹, respectively, corresponding to the D and G band of carbon. The D band is formed due to the degree of structural disorder in carbonaceous materials, and the G band is associated with sp² hybrid carbon representing an ordered graphite crystal of carbon. It is generally believed that the relative intensity (I_D/I_G) of the D band and the G band can be used to characterize the degree of graphitization of the material. The lowest I_D/I_G value (0.63) for GO means higher mode of sp²-bonded carbon atoms for GO because of the p-p stacking by the Van der Waals force[35]. The higher I_D/I_G value for Si/rGO (0.976) indicate that reducing the oxygen groups of GO after heat treatment increase the disorder degree of GO. Furthermore, the I_D/I_G of H-Si@N-C/rGO (1.12) is higher than that of Si/rGO, this might be result from the introduction of dopamine. After heat treatment, the dopamine converted to amorphous carbon structure increase the degree of disordered of carbon, which can also be confirmed by the XRD patterns. In order to prove the chemical bond formation of H-Si@N-C/rGO composites, FT-IR comparative analysis of Si, GO, Si/rGO, H-Si@PDA, H-Si@N-C/rGO was carried out. As shown in Fig. 2d, the region from 3630 cm⁻¹ to 3010 cm⁻¹ represents a hydrogen bond region, and the broad peak appearing at around 3400 cm⁻¹ corresponds to the stretching vibration of -OH. The peaks at 1734 and 1382 cm⁻¹ correspond to the stretching vibration of C=O of the carboxyl group on GO and the bending vibration of O-H. For the H-Si@N-C/rGO and Si/rGO composites, the both C=O peaks are weakened, indicating that the most of oxygen groups of GO are removed at high temperature. The peak at 1043 cm⁻¹ is caused by the stretching vibration of C-OH in GO, which also proves that GO is reduced in H-Si@N-C/rGO and Si/rGO composites. The peak at 1631 cm⁻¹ corresponds to the C=C stretching vibration on the benzene ring, which was previously reported to be due to the C=O stretching vibration of the amide[36]. The peak at 1085 cm⁻¹ corresponds to the Si-O-Si stretching vibration, which is caused by the thermal reduction of magnesium and the hydrothermal process, but the peak intensity of H-Si@N-C/rGO is significantly lower than H-Si@PDA, indicating that the PDA was successfully coated on the silicon surface[37].

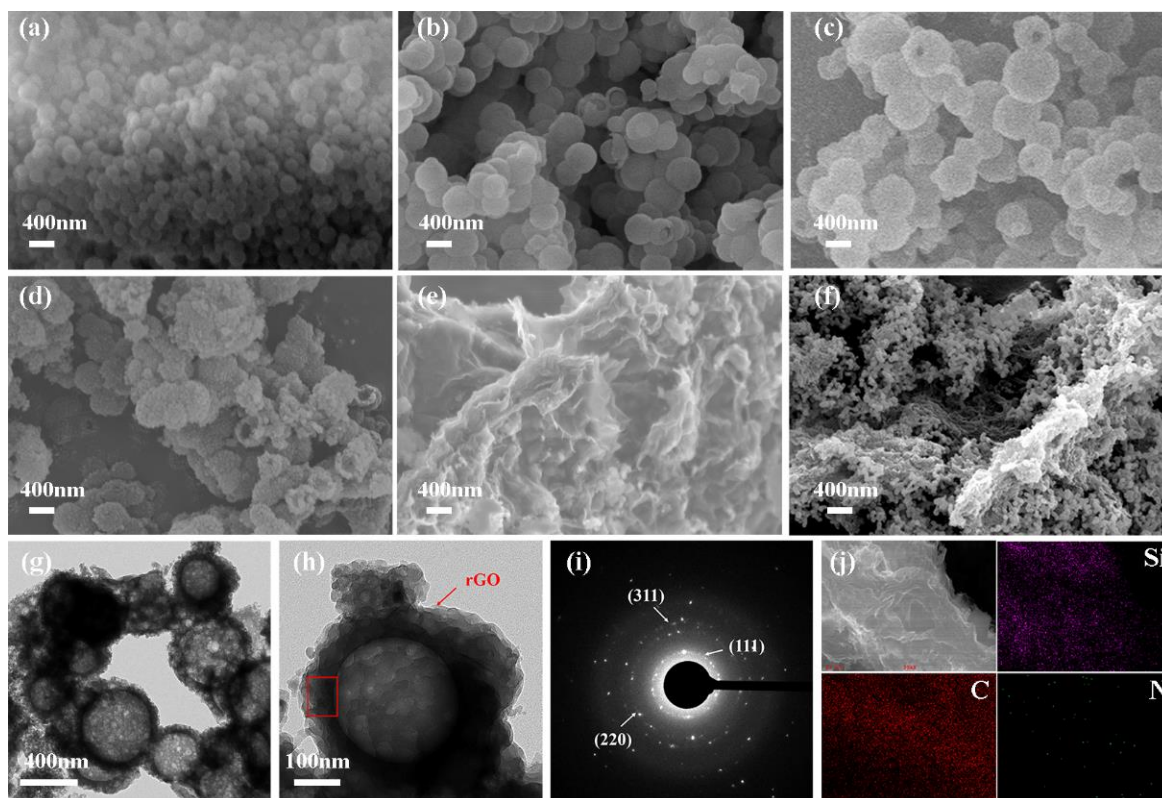


Figure 3. SEM images of (a) carbon sphere, (b) $C@SiO_2$, (c) $H-SiO_2$, (d) $H-Si$ and (e) $H-Si@N-C/rGO$; (f) Si/rGO ; (g) low magnification and (h) high magnification TEM of $H-Si@N-C/rGO$; (i) the SEAD of mapping images of $H-Si@N-C/rGO$, (j) the appearance of Si, C and N element detected from the surface of $H-Si@N-C/rGO$.

The morphology of $H-Si@N-C/rGO$ and its intermediate products are shown in Fig.2. Carbon spheres prepared by the hydrothermal synthesis (Fig.3a) have a smooth sphere surface with the particle size of about 200 nm. The $C@SiO_2$ sphere (Fig.3b) prepared by hydrolysis of TEOS under alkaline environment shows the same sphere as original carbon sphere but with larger particle size of about 400 nm. The larger particles sizes of $C@SiO_2$ means a thickness SiO_2 layers coated on the surface of carbon spheres. After removal of carbon, the $H-SiO_2$ (Fig.3c) still presents the same sphere sizes with $C@SiO_2$. The hollow structure can be confirmed by the cracked SiO_2 spheres. Further, after removal of carbon template, the $H-Si$ are obtained by magnesiothermic reduction which shown is Fig.3d. It can be clearly seen that $H-Si$ still remained as sphere structure with the same particles sizes with $C@SiO_2$. However, most of surface of $H-Si$ are obviously more rouge and loose. Some hollow spheres crack due to the dramatic conversion thermal reaction. The SEM of finally $H-Si@N-C/rGO$ composite after coating with carbon and mixing with rGO are seen in Fig.3e. Most of the $H-Si$ are wrapped in the graphene nanosheets without exposed particles, indicating that the carbon layer along with graphene framework function as a fishing net to protect and encapsulate the $H-Si$ particles. The coverage of graphene might result from electrostatic self-assembly combination of graphite oxide with $H-Si$ at exist of CTAB on the surface of $H-Si$ [38]. On the contrary, the Si/rGO composites without CTAB at the same hydrothermal process display random agglomerate of nano-Si particles on the surface of graphene structure (Fig.3f). The TEM

of H-Si@N-C/rGO (Fig.3g) further confirmed the hollow structure of silicon. In addition, it can be clearly seen that hollow silicon shell are composed of numerous Si nanocrystals with intragranular voids between the particles. Meanwhile, the graphene layer tightly covered the shell of hollow silicon (Fig.3h). The corresponding region of hollow silicon presents three diffraction rings (Fig.3i), which index to the (111), (220), (311) plane of Si. The result also indicates that the silicon convert from magnesiothermic reduction has the poly-crystalline structure. The appearance of Si and C elements in mapping image of H-Si@N-C/rGO (Fig.3j) demonstrate that silicon particles are uniform distributed in the graphene structure. The existence of N element in the mapping image of H-Si@N-C/rGO is result from the carbonization of polydopamine which introduction of N into carbon structure[39].

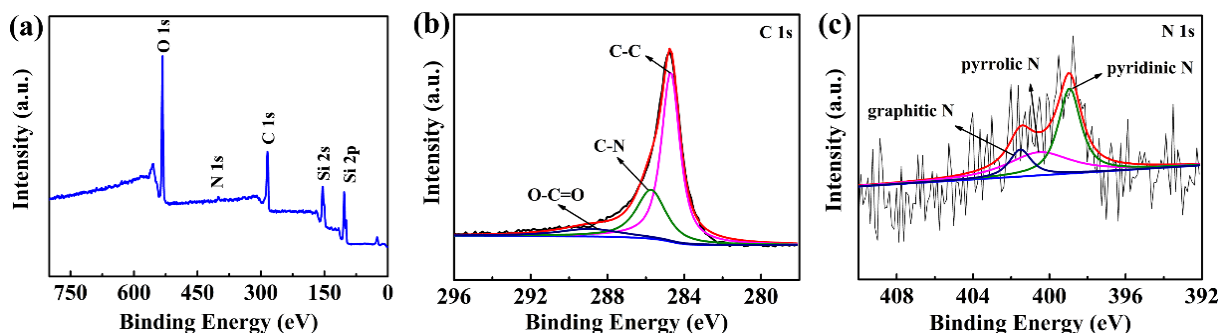


Figure 4. XPS spectrum of (a) H-Si@ N-C/rGO and (b-c) C1s and N1s in H-Si@ N-C/rGO.

The elemental information of the H-Si@ N-C/rGO composite was further characterized by XPS analysis. In Fig. 4a, the C, Si, O and N elements can be detected in the complete XPS spectrum of H-Si@ N-C/rGO. In the C 1s spectrum of H-Si@ N-C/rGO (Fig.4b), it can be divided into three peaks of 284.7, 285.7 and 288.6 eV, corresponding to the C-C, C-N and O-C=O bonds. The existence of C-N might due to amide groups by the polydopamine[40]. In addition, the small peaks of O-C=O bonds indicates that the most of the oxygen groups of graphite oxide has been removed after heat treatment, which is also agree with the pervious FTIR result. The high-resolution N 1s spectrum indicates that the N atom exists in the form of pyridine N, pyrrole N and graphite N, which further proved that PDA is successfully coated on the silicon surface[41].

Table 1. Surface area and total pore volume of Si, Si/rGO and H-Si@N-C/rGO

Samples	S_{BET} ($\text{m}^2 \text{g}^{-1}$) ^a	S_{BJH} ($\text{m}^2 \text{g}^{-1}$) ^b	V_{total} ($\text{cm}^3 \text{g}^{-1}$) ^c	V_{BJH} ($\text{cm}^3 \text{g}^{-1}$) ^d
H-Si@N-C/rGO	140.6	163.9	0.40	0.87
Si/rGO	84.9	62.8	0.31	0.08
Si	48.7	41.5	0.11	0.11

a The BET surface areas (S_{BET}) are derived using multipoint BET method.

b The BJH adsorption cumulative surface area of pores between 1 nm and 300 nm diameter.

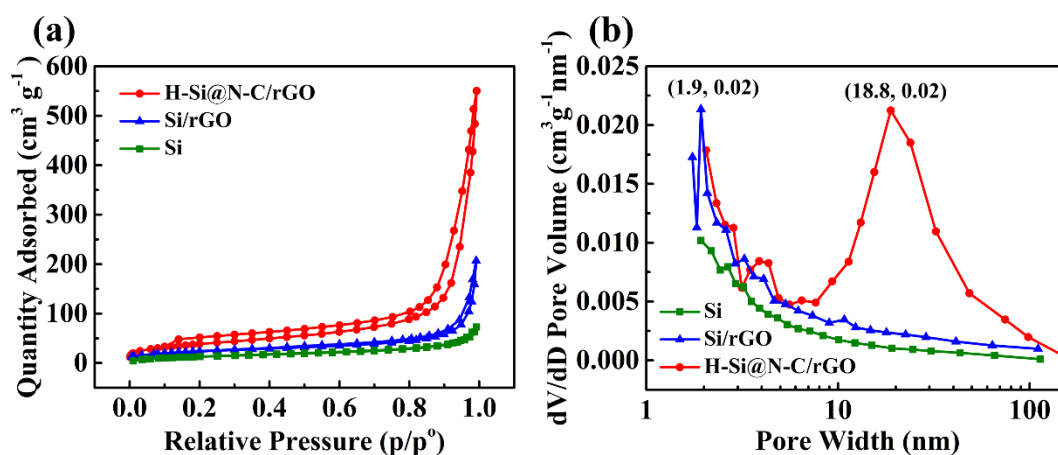
c Total pore (< 250 nm) volume (V_{total}) was estimated from the amount adsorbed at a relative pressure P/P^0 of 0.99.

d The BJH adsorption cumulative volume of pores between 1 nm and 300 nm diameter.

Table 2. Parameters of equivalent circuit from fitting the impedance spectra.

Samples	$R_e(\Omega)$	$R_f(\Omega)$	$R_{ct}(\Omega)$	$W(\Omega \text{ s}^{-1/2})$	CPE1(F)	CPE2(F)
After first cycle						
H-Si@N-C/rGO	3.7	19.3	4.2	0.4	1.5E-4	1.46E-6
Si/rGO	3.2	17.5	103.1	0.5	2.5E-4	0.029
Si	3.8	6.2	33.0	0.5	7.9 E-4	0.005
After 50 cycles						
H-Si@N-C/rGO	3.2	29.4	6.5	0.4	2.0E-4	0.024
Si/rGO	3.3	66.2	117.4	0.4	1.1E-4	0.003
Si	4.6	56.8	36.9	0.4	1.2 E-4	0.001

To further investigate the pore structure of the composite, the nitrogen adsorption/desorption curves and pore size distributions of Si, Si/rGO and H-Si@ N-C/rGO were measured, as shown in Fig.5. Both Si/rGO and H-Si@ N-C/rGO have type IV isotherm of H4 hysteresis loop, while Si is a type II isotherm, which verified pore structure caused by the stacking of rGO and the magnesium thermal reduction process. As shown in Table 1, the calculated Brunauer-Emmett-Teller (BET) surface areas of Si, Si/rGO, and H-Si@ N-C/rGO were 48.7, 84.9, and 140.6 m²/g, respectively. The higher BET surface area of H-Si@N-C/rGO is attributed to the removal of pores left by the magnesium oxide after reduction. Due to the stacking of the rGO sheets, the specific surface area of Si/rGO is larger than that of Si. In addition, the pore volumes of H-Si@N-C/rGO and Si/rGO are 0.4 and 0.31 cm³/g, respectively, which are much larger than Si (0.11 cm³/g), indicating that magnesiothermic reduction and the graphene oxide stack form abundant pores. The pore size distribution of the three materials can be observed from Fig. 5 b. The peak of Si/rGO appears at 1.9 nm, due to the rGO stacking. H-Si@ N-C/rGO has a small peak at ~4nm, which result from the disordered stacking between garphene nanosheets and H-Si. In addition, H-Si@ N-C/rGO has another broad peak between 10-50 nm, resulting from the hollow structure of Si after the magnesiothermic reduction. The multilevel pore structures not only buffer the volume expansion of silicon during the charge/discharge process, but also provide a fast channel for lithium ion and electron transport[42].

**Figure 5.** (a) nitrogen adsorption and desorption curve; (d) pore size distribution curves of Si, Si/rGO, and H-Si@N-C/rGO.

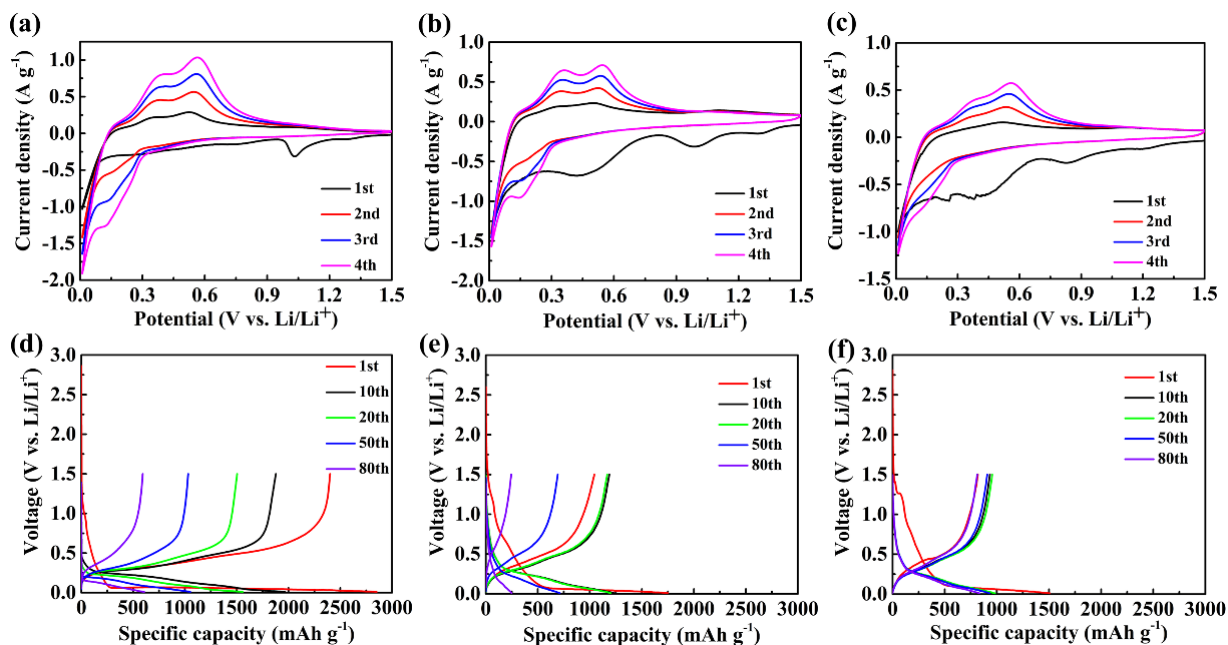


Figure 6. CV curves of (a) Si, (b) Si/rGO and (c) H-Si@N-C/rGO; Galvanic discharge-charge curves of (d) Si, (e) Si/rGO and (f) H-Si@N-C/rGO.

The electrochemical performance of Si, Si/rGO and H-Si@N-C/rGO are firstly investigated by the CV curves at a scan rate of 0.5 mV s^{-1} in the potential range of 0.01-1.5 V. A significant cathode peak appeared at 1.03 V (vs Li/Li^+) in the first cycle for the CV curve of Si (Fig.6a), and disappeared in the subsequent cycles, corresponding to the decomposition of the electrolyte to form an SEI film on the surface of the Si electrode. In the subsequent cycle, a significant cathodic peak appeared below 0.2 V due to the formation of a Li_xSi alloy, which corresponds to lithium ion intercalation, which is a typical peak of the Si anode electrode[43]. The anodic peaks of 0.3 V and 0.5 V are the result of Li^+ removed from the Li_xSi alloy. In the subsequent cycle, the peak intensity gradually increased, indicating that Si gradually activated. The CV curves of Si/rGO and H-Si@N-C/rGO have similar phenomena, but a broad peak appears at 0.2-0.7 V compared with pure Si. It is results from the presence of rGO, which increase the specific surface area of electrode (S_{BET}) and more side reaction to consume electrolyte to formation of SEI films at the initial discharge process[44]. Fig.6 (d-f) show the galvanic charge/discharge curve of the electrodes Si, Si/rGO and H-Si@N-C/rGO at the current density of 0.2 A g^{-1} in the voltage range of 0.01-1.5 V (vs. Li/Li^+), respectively. It is observed in Fig.6d that an oblique curve appears in the initial discharge interval of about 1.0 V to 0.1 V, which is the formation of the SEI film. A voltage platform of less than 0.1 V appears during the first discharge, which indicates lithium ions are embedded in the crystalline Si to form a LiSi_x alloy. After the first cycle, the voltage profile of the discharge curve increases to 0.28 V, which may be related to the lithiation of amorphous silicon. A similar phenomenon was observed in Fig. 6 (e, f). It shows that the addition of rGO does not affect the redox reaction of Si. It can be clearly seen from Fig. 6 (d-f) that the polarization of the galvanic charge-discharge curve for H-Si@N-C/rGO is much smaller those of Si and Si/rGO under different cycle times, indicating the interface of Si and electrolyte retain stable during the cycles[45].

The cycling performance of Si, Si/rGO and H-Si@N-C/rGO are investigated by galvanostatic discharge-charge measurement at a current density of 0.2 A g^{-1} . The weight of active materials are based on whole Si and carbon. The initial charge/discharge specific capacities of H-Si@N-C/rGO are 818/1508 mAh g^{-1} with coulomb efficiency of 54.2%. The large irreversible capacity loss is consistent with the results of the CV curve, resulting from the large specific surface area of H-Si@N-C/rGO and the formation of SEI film, which also seen in lots of literatures[46-48]. However, after three cycles, the coulombic efficiency of H-Si@N-C/rGO rapidly increased to 93%, and after 15 cycles, the coulombic efficiency was stable above 97%. After 100 cycles, the H-Si@N-C/rGO charge specific capacity was maintained at 731 mAh/g with the initial capacity retention rate of 89.4%. For comparison, under the same electrochemical conditions, the initial charge/discharge capacities of Si/rGO and Si are about 1075/1786 mAh g^{-1} and 2401/2851 mAh g^{-1} , respectively, but their capacity decays rapidly after 100 cycles, only maintained at 169 mAh g^{-1} and 300 mAh g^{-1} , the capacity retention rates were 15.7% and 12.5%, respectively. The rate performance of the three samples are further tested. As shown in Fig. 6b. The H-Si@N-C/rGO electrode displays reversible capacity of 790, 694, 602 and 461 mAh/g at high current densities of 1 A g^{-1} , 2 A g^{-1} , 3 A g^{-1} and 5 A g^{-1} . However, under the same conditions, the capacity of the Si electrode has been decayed to near zero after 1 A g^{-1} , which are result from pulverization of electrode after large volume expansion. For the Si/rGO electrode, although it exhibits higher rate capability at smaller current density, it still suffers rapid capacity decrease at higher current density, indicating that the single graphene cannot guarantee high effective conductive transport. This is also consistence with the SEM of Si/rGO (Fig. 2f). On the contrary, taking the advantages of synergetic protection of coating carbon layer and graphene nanosheets, the hollow Si can be maintained stable conductive framework.

Table 3. The electrochemical performance of typical Si/graphene based composites for lithium ion battery

Samples	Potential cut-off (V)	Cycle number	Specific discharge capacity (mAh g^{-1})	Current density (mA g^{-1})	Ref.
H-Si@N-C/rGO	0.01-1.5	150	608	1000	This work
		100	818	200	
Si-C-rGO	0.01-1	100	765	200	[42]
rGO-Si-CNT	0.01-1.5	-	550	1000	[49]
Si/HC/G	0.01-2	-	547	1000	[50]
Si@void@C	0.01-1	100	510	1000	[51]
Si/MWCNT/Graphene	0.01-2	500	695	200	[52]
Si-G-PANI	0.01-1	100	721	1000	[53]
Si/GS/C-S@Gr	0.02-1.5	200	600-620	200	[54]

At the meantime, the volume expansion can also be suppressed by the multilevel of mesoporous structure in the Si nanocrystals as well as the hollow structure. As a result, H-Si@N-C/rGO displays much better cycling stability and rate performance than those of Si/rGO. Fig.7c also shows the cycling performance of the H-Si@N-C/rGO electrode at high current density of 1 A g^{-1} . The initial reversible

capacity is 660 mAh g⁻¹ with the coulombic efficiency of 95% after 3 cycles and finally retained at 608 mAh g⁻¹ after 150 cycles. The capacity retention rate is 92 % of initial charge capacity with high coulombic efficiency stable at 98.4%. Compare with other similar Si graphene based composites for lithium ion battery [42, 49-54], As shown in Table 3, the H-Si@N-C/rGO still displays comparable electrochemical performance at cycling stability and reversible capacity under the lower and higher current density.

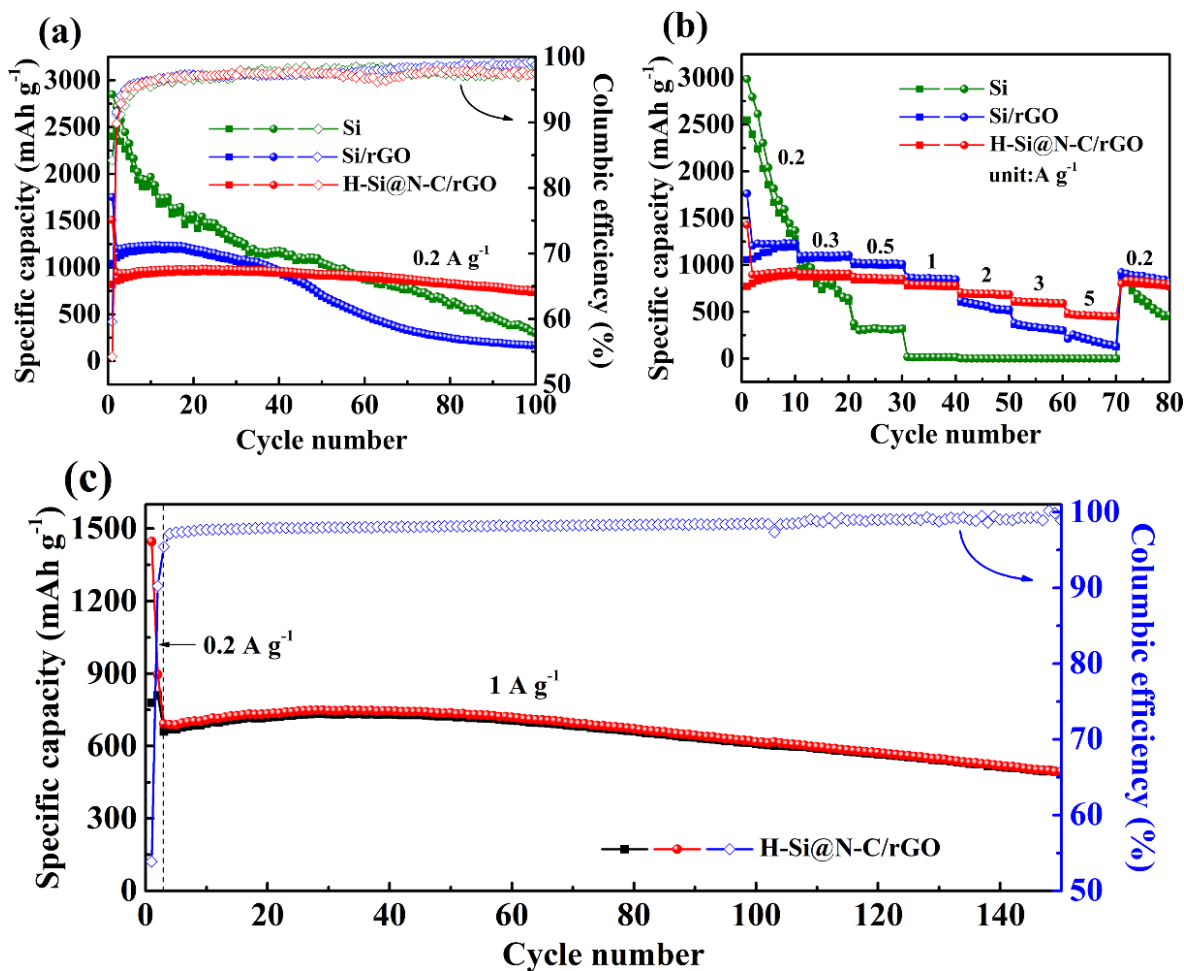


Figure 7. (a) cycling performance of Si, Si/rGO and H-Si@N-C/rGO at a current density of 0.2 A/g; (b) rate performance of Si, Si/rGO and H-Si@N-C/rGO at different current densities. (c) The cycle performance of H-Si@N-C/rGO was tested with 1 A/g after two cycles of 0.2 A/g. (The load masses of the electrodes Si, Si/rGO and H-Si@N-C/rGO are 0.55 mg/cm², 0.55 mg/cm², 0.55 mg/cm², respectively).

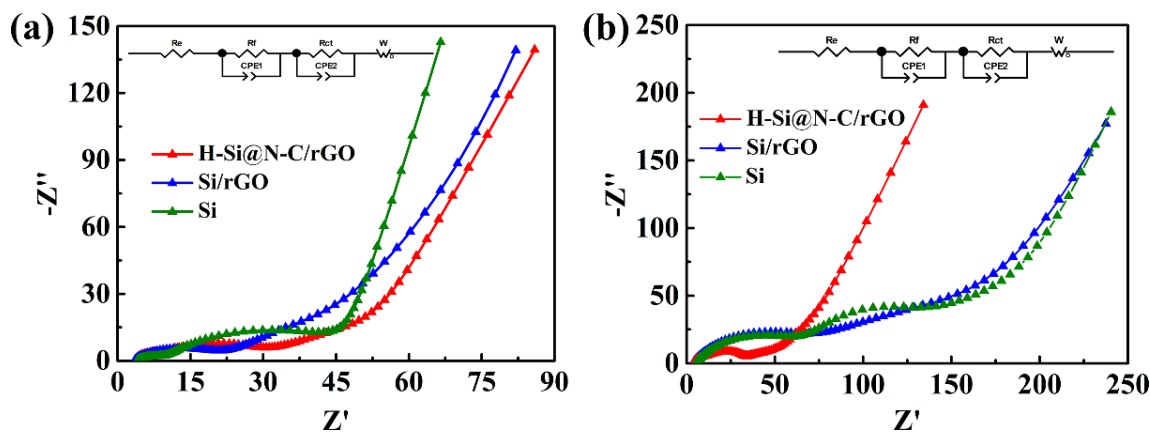


Figure 8. Nyquist plots of the Si, Si/rGO and H-Si@N-C/rGO electrodes measured a) after 1 cycle and b) 50 cycles.

To further explain the difference of electrochemical performance of the Si, Si/rGO and H-Si@N-C/rGO electrodes, the electrochemical impedances of the three electrodes after the first cycle and after 50 cycles were tested at the discharge state. After the first cycle, the R_f of H-Si@N-C/rGO (19.3Ω) and Si/rGO (17.5Ω) is significantly higher than that of Si (6.2Ω) due to their larger specific surface area, resulting in more electrolyte decomposition forming a SEI film on the surface of the material. This result is consistent with the results of their initial coulombic efficiency. However, after 50 cycles, the R_f of H-Si@N-C/rGO is 29.4Ω with a little increase compared with the first cycles, but much lower than those of Si (56.8Ω) and Si/rGO (66.2Ω), indicating that H-Si@N-C/rGO can form a more stable SEI film. The stable interface between active materials and electrolyte is ascribed to the dual protection of carbon layer as well as graphene nanosheets. In addition, the intragranular voids between the particles along with the hollow Si structure reduce the mechanical stress during the cycling process, also increase the stability of structure. Furthermore, the R_{ct} value of H-Si@N-C/rGO is 4.2Ω after 1st cycles, which is significantly smaller than that of Si (33Ω) and Si/rGO (103.1Ω). And the R_{ct} of H-Si@N-C/rGO (6.5Ω) also exhibits little increase after 50 cycles, compared with Si (36.9Ω) and Si/rGO (117.4Ω). This result reflects the synergistic function of carbon layer and graphene nanosheets, which improves the interfacial contact between the silicon particles and the electrolyte, finally promotes the charge transfer process [55]. On the other hand, the nitrogen-doped carbon also significantly improves the electronic conductivity and the Li^+ diffusion coefficient.

4. CONCLUSIONS

In this work, we successfully prepared hollow silicon using carbon as a hard template in combination of magnesiothermic reduction. Further, taking advantages of dual carbon protecting silicon, we fabricated hollow Si@nitrogen-doped carbon/reduced graphene oxide composites to synergistically improve the electrochemical stability as lithium-ion battery anode. The hollow Si structure can suppress the large volume change because of the multilevel intragranular voids between the particles along with the hollow structure. The nitrogen-doped carbon layer also improves the electronic conductivity and the

Li⁺ diffusion coefficient due to more free electrons in the carbon structure. In addition, the dual-carbon protecting by nitrogen-doped carbon/reduced graphene oxide also construct stable electrode interface and conductive framework during cycling process. As a result, the hollow Si@ nitrogen-doped carbon/reduced graphene oxide composites displays stable electrochemical performance at high current density as well as comparable rate performance. The strategy of design hollow structure along with carbon protection provide a feasible method for other high capacity electrode materials with large volume change toward practical lithium-ion battery applications.

ACKNOWLEDGEMENTS

This work was supported by the National Natural Science Foundation of China (Grant No. 51604250, 51502250, 51474196), the Science & Technology Department of Sichuan Province (Grant No. 2017JQ0044, 2019YFG0220), Youth Science and Technology Innovation Team of Energy Material Electrochemistry of Southwest Petroleum University (grant No.2015CXTD04), and Undergraduate Innovation and Entrepreneurship Program (grant No.201710615031).

References

1. J.B. Goodenough, *Energy Storage Mater.*, 1 (2015) 158.
2. C. Liu, F. Li, L.-P. Ma and H.-M. Cheng, *Adv. Mater.*, 22 (2010) E28.
3. M. Armand, J.M. Tarascon, *Nature*, 451 (2008) 652.
4. W.J. Zhang, *J. Power Sources*, 196 (2011) 13.
5. M.N. Obrovac and V.L. Chevrier, *Chem. Rev.*, 114 (2014) 11444.
6. U. Kasavajjula, C. Wang and A.J. Appleby, *J. Power Sources*, 163 (2007) 1003.
7. K. Feng, M. Li, W. Liu, A.G. Kashkooli, X. Xiao, M. Cai and Z. Chen, *Small*, 14 (2018) 1702737.
8. J.W. Choi and D. Aurbach, *Nat. Rev. Mater.*, 1 (2016) 16.
9. K.Q. Peng, X. Wang, L. Li, Y. Hu and S.T. Lee, *Nano Today*, 8 (2013) 75.
10. J. Liu, G. Cao, Z. Yang, D. Wang, D. Dubois, X. Zhou, G.L. Graff, L.R. Pederson and J.-G. Zhang, *ChemSusChem*, 1 (2008) 676.
11. X. Su, Q. Wu, J. Li, X. Xiao, A. Lott, W. Lu, B.W. Sheldon and J. Wu, *Adv. Energy Mater.*, 4 (2014) 1300882.
12. T. Yoon, T. Bok, C. Kim, Y. Na, S. Park and K.S. Kim, *ACS Nano*, 11 (2017) 4808.
13. J. Zhu, J. Yang, Z. Xu, J. Wang, Y. Nuli, X. Zhuang and X. Feng, *Nanoscale*, 9 (2017) 8871.
14. N. Liu, X. Mamat, R. Jiang, W. Tong, Y. Huang, D. Jia, Y. Li, L. Wang, T. Wågberg and G. Hu, *Chem. Eng. J.*, 343 (2018) 78.
15. C.-H. Jung, J. Choi, W.-S. Kim and S.-H. Hong, *J. Mater. Chem. A*, 6 (2018) 8013.
16. K. Mishra, J. Zheng, R. Patel, L. Estevez, H. Jia, L. Luo, P.Z. El-Khoury, X. Li, X.-D. Zhou and J.-G. Zhang, *Electrochim. Acta*, 269 (2018) 509.
17. T.M. Higgins, S.H. Park, P.J. King, C.J. Zhang, N. Mcevoy, N.C. Berner, D. Daly, A. Shmeliov, U. Khan and G. Duesberg, *ACS Nano*, 10 (2016) 3702.
18. H. Wu, G. Yu, L. Pan, N. Liu, M.T. McDowell, Z. Bao and Y. Cui, *Nat. Commun.*, 4 (2013) 1943.
19. D. Liu, Y. Zhao, R. Tan, L.-L. Tian, Y. Liu, H. Chen and F. Pan, *Nano Energy*, 36 (2017) 206.
20. C.H. Hsu, H.H. Lin, Y.H. Liu and H.P. Lin, *New J. Chem.*, 42 (2018) 9058.
21. Y.L. Chen, Y. Hu, J.Z. Shao, Z. Shen, R.Z. Chen, X.W. Zhang, X. He, Y.Z. Song and X.L. Xing, *J. Power Sources*, 298 (2015) 130.
22. X. Wang, G. Li, M.H. Seo, G. Lui, F.M. Hassan, K. Feng, X. Xiao and Z. Chen, *ACS Appl. Mater. Interfaces*, 9 (2017) 9551.
23. D.S. Tan, B. Liu, D. Chen and G.Z. Shen, *RSC Adv.*, 4 (2014) 18391.
24. Q. Si, M. Kawakubo, M. Matsui, T. Horiba, O. Yamamoto, Y. Takeda, N. Seki and N. Imanishi, *J. Power Sources*, 248 (2014) 1275.

25. H.C. Tao, L.Y. Xiong, S.C. Zhu, X.L. Yang and L.L. Zhang, *Int. J. Hydrogen Energy*, 41 (2016) 21268-21277.
26. J. Chang, X. Huang, G. Zhou, S. Cui, S. Mao and J. Chen, *Nano Energy*, 15 (2015) 679.
27. M.L. Jiao, J. Qi, Z.Q. Shi and C.Y. Wang, *J. Mater. Sci.*, 53 (2018) 2149.
28. M. Su, H. Wan, Y. Liu, W. Xiao, A. Dou, Z. Wang and H. Guo, *Powder Tech.*, 323 (2018) 294.
29. S. Chen, L. Shen, P.A. van Aken, J. Maier and Y. Yu, *Adv. Mater.*, 29 (2017) 1605650.
30. C. Fang, Y. Deng, Y. Xie, J. Su and G. Chen, *J. Phys. Chem. C*, 119 (2015) 1720.
31. R.-a. Huang, Y. Guo, Z. Chen, X. Zhang, J. Wang and B. Yang, *Ceram. Int.*, 44 (2018) 4282.
32. M. Wang, Y. Ma, J. Jiang, Y. Huang, X. Li, J. Zheng, C. Qin, P. Yan and G. Cao, *ChemElectroChem*, 6 (2019) 1139.
33. D.A. Agyeman, K. Song, G.H. Lee, M. Park and Y.M. Kang, *Adv. Energy Mater.*, 6 (2016) 1600904.
34. M.-S. Wang, G.-L. Wang, S. Wang, J. Zhang, J. Wang, W. Zhong, F. Tang, Z.-L. Yang, J. Zheng and X. Li, *Chem. Eng. J.*, 356 (2019) 895.
35. M.-S. Wang, Z.-Q. Wang, Z.-L. Yang, Y. Huang, J. Zheng and X. Li, *Electrochim. Acta*, 240 (2017) 7.
36. X. Zhang, L. Tao, P. He, X. Zhang, M. He, F. Dong, S. He, C. Li, H. Liu, S. Wang and Y. Zhang, *Electrochim. Acta*, 259 (2018) 793.
37. C. Liu, J. Wang, J. Li, R. Luo, J. Shen, X. Sun, W. Han and L. Wang, *ACS Appl. Mater. Interfaces*, 7 (2015) 18609.
38. H. Liu, Z. Shen, S. Liang, L. Liu, M. Yi, X. Zhang and S. Ma, *New J. Chem.*, 40 (2016) 7053.
39. Y. Zhou, H. Guo, Y. Yong, Z. Wang, X. L and R. Zhou, *Mater. Lett.*, 195 (2017) 164.
40. Y. Bie, J. Yang, X. Liu, J. Wang, Y. Nuli and W. Lu, *ACS Appl. Mater. Interfaces*, 8 (2016) 2899.
41. R. Zhou, H. Guo, Y. Yang, Z. Wang, X. Li and Y. Zhou, *J. Alloy. Compd.*, 689 (2016) 130.
42. J. Wu, X. Qin, H. Zhang, Y.-B. He, B. Li, L. Ke, W. Lv, H. Du, Q.-H. Yang and F. Kang, *Carbon*, 84 (2015) 434.
43. M.-S. Wang, Z.-Q. Wang, R. Jia, Y. Yang, F.-Y. Zhu, Z.-L. Yang, Y. Huang, X. Li and W. Xu, *Appl. Surf. Sci.*, 456 (2018) 379.
44. X. Cai, W. Liu, Z. Zhao, S. Li, S. Yang, S. Zhang, Q. Gao, X. Yu, H. Wang and Y. Fang, *ACS Appl. Mater. Interfaces*, 11 (2019) 3897.
45. X. Li, K. Zhang, M. Wang, Y. Liu, M. Qu, W. Zhao and J. Zheng, *Sustain. Energy Fuels*, 2 (2018) 413.
46. M.H. Lin, S. Hy, C.Y. Chen, J.H. Cheng, J. Rick, N.W. Pu, W.N. Su, Y.C. Lee and B.J. Hwang, *ChemElectroChem*, 3 (2016) 1446.
47. F. Zhang, X. Yang, Y. Xie, N. Yi, Y. Huang and Y. Chen, *Carbon*, 82 (2015) 161.
48. E. Greco, G. Nava, R. Fathi, F. Fumagalli, A.E. Del Rio-Castillo, A. Ansaldo, S. Monaco, F. Bonaccorso, V. Pellegrini and F. Di Fonzo, *J. Mater. Chem. A*, 5 (2017) 19306.
49. M. Fang, Z. Wang, X. Chen and S. Guan, *Appl. Surf. Sci.*, 436 (2018) 345.
50. M. Jiao, J. Qi, Z.-Q. Shi and C.-Y. Wang, *J. Mater. Sci.*, 53(2018) 2149.
51. M. Mi, X. Yang, Y. Li, P. Zhang and L. Sun, *Chem. Eng. J.* 351(2018) 103.
52. G. Hatipoglu, M. Alaf and H. Akbulut, *J. Mater. Sci.: Mater. El.*, 30 (2019) 2067.
53. H. Mi, F. Li, C. He, X. Chai, Q. Zhang, C. Li, Y. Li and J. Liu, *Electrochim. Acta*, 190 (2016) 1032.
54. N. Kim, C. Oh, J. Kim, J. Kim, E. D. Jeong, J.-S. Bae, T. E. Hong and J. K. Lee, *J. Electrochem. Soc.*, 164 (2017) 6075.
55. J. Wang, D.-H. Liu, Y.-Y. Wang, B.-H. Hou, J.-P. Zhang, R.-S. Wang and X.-L. Wu, *J. Power Sources*, 307 (2016) 738.